PCCP

Accepted Manuscript

ROYAL SOCIETY OF CHEMISTRY

www.rsc.org/pccp

Physical Chemistry Chemical Physics RSCPublishing

ARTICLE

Sputtering graphite coating to improve the elevated-temperature cycling ability of $LiMn_2O_4$ electrode †

Cite this: DOI: 10.1039/xoxxoooooox

Jiexi Wang,[a,#] Qiaobao Zhang,[b,#] Xinhai Li,[a,&] Zhixing Wang,[a] Huajun Guo,[a] Daguo Xu[b] and Kaili Zhang[b,&]

Received ooth January 2014,
Accepted ooth January 2014

DOI: 10.1039/xoxxoooooox

www.rsc.org/

To improve the cycle performance of $LiMn_2O_4$ at elevated temperature, a graphite layer is introduced to directly cover the surface of commercial $LiMn_2O_4$-based electrode via room-temperature DC magnetron sputtering. The as-modified cathodes display improved capacity retention as compared to the bare $LiMn_2O_4$ cathode (BLMO) at 55 °C. When sputtering graphite for 30 min, the sample shows the best cycling performance at 55 °C, maintaining 96.2% capacity retention after 200 cycles. Reasons with respect to the graphite layer for improving the elevated-temperature performance of $LiMn_2O_4$ are systematically investigated via the methods of cyclic voltammetry, electrochemical impedance spectroscopy, X-ray photoelectron spectrometry, scanning and transmission electron microscopy, X-ray diffraction and inductively coupled plasma-atomic emission spectrometry. The results demonstrate that the graphite coated $LiMn_2O_4$ cathode has much less increased electrode polarization and electrochemical impedance than BLMO during the elevated-temperature cycling process. Furthermore, the graphite layer is able to alleviate the severe dissolution of manganese ions into the electrolyte and mitigate the morphological and structural degradations of $LiMn_2O_4$ during cycling. A model for electrochemical kinetics process is also suggested for explaining the roles of the graphite layer on suppressing the Mn dissolution.

1 Introduction

Lithium ion batteries (LIBs) with high energy and power density capability have attracted widespread attention as these batteries show great promise as the dominant power sources for portable electronics.[1, 2] Spinal $LiMn_2O_4$ has been considered as one of the most attractive materials to replace layered $LiCoO_2$ as potential cathode for being used in LIBs due to its low cost, non-toxicity, high safety and high power density.[3-6] However, the severe capacity fading particularly at elevated temperature (50-60 °C), which is caused by many reasons such as Jahn-Teller transition, formation of traces of HF leading to Mn leaching, and continuous decomposition of electrolyte on the electrode, should be solved urgently to realize the application of $LiMn_2O_4$-based cathodes in commercial LIBs.[7-11] To solve this problem, many strategies have been developed including in the doping of $LiMn_2O_4$ with metal cations,[4, 5, 12-16] the surface modification of $LiMn_2O_4$ particles by more stable materials,[17-21] and the introduction of artificial protective coating layer on the surface of $LiMn_2O_4$ cathode.[22-26] Elemental doping can enhance the stability of the crystal structure of $LiMn_2O_4$ and restrain the Jahn-Teller transition.[16, 27] However, it is difficult to improve the stability of the electrode-electrolyte interface via metal doping. Surface coating is a feasible and effective technology to improve the performance of $LiMn_2O_4$ by virtue of modifying the surface chemical stability or providing a protective layer to minimize the direct contact of the active material with the electrolyte.[18, 28, 29] In this regard, electro-inert and structurally stable species, such as metal oxides, phosphates, fluorides, etc., have been used to coat on the surface of $LiMn_2O_4$ particles.[30] These researches have indicated that surface coating can serve as HF scavenger to reduce the electrolyte acidity, and thus slow down the dissolution of manganese ions and the degradation of the electrolyte on the cathode, leading to improved elevated-temperature performance of $LiMn_2O_4$. However, the most introduced oxide or nonoxide coatings usually have poor electronic conductivity. The electro-active materials have also been introduced to coat the $LiMn_2O_4$ particles and have shown positive effects on improving the elevated-temperature performance.[31, 32] Nevertheless, this strategy is often conducted with wet chemical methods and the coating thickness and quantity are not easy to be well controlled.[22]

It is believed that the poor elevated-temperature performance of spinel $LiMn_2O_4$ is mainly attributed to deleterious side reaction occurring at the electrode-electrolyte interface.[33] Therefore, it is important to master the chemical stability of $LiMn_2O_4$ electrode with respect to its operating electrolyte medium by controlling the electrode-electrolyte interface.[29] In addition to the active-material-side strategies mentioned above, artificial preparation of a protective layer to directly cover the surface of as-fabricated $LiMn_2O_4$ electrode may be another effective way to enhance the interface stability of the $LiMn_2O_4$ cathode during the elevated-temperature electrochemical cycling.[24] Up to now, the atomic layer deposition of metal oxide coatings directly onto $LiMn_2O_4$ electrodes has been successfully introduced to improve the

elevated-temperature cycle performance of $LiMn_2O_4$-based LIBs.[23, 25, 26, 34] These protective metal oxide coatings on the surface of $LiMn_2O_4$ cathode can serve as an effective HF scavenger to suppress Mn dissolution.

However, as compared to metal oxide coatings, carbon materials own several desirable features arising from its unique chemical and physical properties.[29, 35] Particularly, metal oxides commonly have poor electronic conductivity, while the graphite has high electronic conductivity and can be acted as a good conductive medium for charge transmission.[35] Up to now, carbon coating has been intensively investigated as an effective way to improve the electrochemical performance of the electrode materials for LIBs.[29, 35] Although the carbon coated- $LiMn_2O_4$ and $LiMn_2O_4$/C composites have shown enhanced rate capability, to the best of our knowledge, there is no literature to report the improvement in elevated-temperature cycle performance of carbon modified $LiMn_2O_4$ cathode. Moreover, most of the carbon coated- $LiMn_2O_4$ and $LiMn_2O_4$/C composites were prepared by diverse chemical procedures such as sol-gel, hydrothermal and high-temperature decomposition methods. These methods can result in detrimental effects on the $LiMn_2O_4$ structural stability and thus lead to poor electrochemical performance at elevated temperature.[36-38] Furthermore, it is difficult to control the thickness as well as the uniformity of the carbon coatings by using these methods.[35] Compared to the chemical procedures, physical methods, such as physical vapour deposition[35] and magnetron sputtering,[39, 40] have been proved to be the alternative carbon coating procedures due to a fact that these methods can be carried out at room temperature and the thickness and uniformity of the as-prepared carbon layer can be well controlled. Magnetron sputtering as a simple but effective physical deposition technology, which can be conducted at room temperature, has become the process of choice for the deposition of a wide range of important coatings.[41] More importantly, this method does not need heat treatment and thus protect the spinal structure of $LiMn_2O_4$ from damaging. Otherwise, the Mn^{4+} and Mn^{3+} can be reduced by heating in such reducing atmosphere.[30] In this work, we introduce a conductive graphite layer directly covering the surface of $LiMn_2O_4$ electrode by magnetron sputtering for enhancing the cycle performance of $LiMn_2O_4$ at elevated temperature. Sputtering time is altered to determine the optimal coating thickness. The roles of graphite physical barrier layer in the improvement of cycle performance of $LiMn_2O_4$-based LIBs at elevated temperature are systematically investigated. The graphite covering layer is desired to act as a barrier between $LiMn_2O_4$ cathode and electrolyte, suppressing the side reactions at the interface including corrosion of electrolyte to $LiMn_2O_4$ particles and then Mn dissolution. Consequently, it is expected to make a remarkable improvement in cycle life at elevated temperature. A kinetic model for the electrochemical process is suggested for explaining the functions of the graphite layer.

2 Experimental

2.1 Sample preparations

The progress of preparation of graphite coated $LiMn_2O_4$ electrodes is graphically presented in Fig. 1. Concretely, the commercial $LiMn_2O_4$ particles (purchased from Hunan Shanshan Toda Advanced Materials Co. Ltd) were mixed with 10 wt.% Super P carbon black and 10 wt.% polyvinylidene fluoride (PVDF) in N-2-methyl pyrrolidone (NMP) until homogeneous slurry was obtained. Then, the blended slurry was cast onto an aluminum current collector, followed by drying at 120 ^oC for 3 h to form the bare $LiMn_2O_4$ electrode (BLMO). After that, the as-prepared positive plate was then treated by deposition of a graphite layer via magnetron sputtering. Prior to deposition, the prepared positive plate was loaded in the sputter chamber, which was vacuumed to approximately 10^{-4} Pa. The distance between the graphite target and substrate was about 120 mm and the substrate holder rotated at a frequency of 4 $rev \cdot min^{-1}$. The growth rate of graphite layer is about 100 nm h^{-1}. The magnetron plasma was excited by DC power (0.4 A, 200 V) and the growth time was 10 (GLMO-10,), 30 (GLMO-30), 60 min (GLMO-60).. The prepared plates were cut into rounded pieces, then dried at 60 ^oC in a vacuum drying oven overnight.

For comparison, the graphite partially coated $LiMn_2O_4$ particles (PGLMO) were also prepared. Prior to magnetron sputtering treatment, the $LiMn_2O_4$ particles were mixed homogeneously with 1 wt.% PVDF in NMP, and then casted onto an aluminum foil followed by drying. After that, it was modified by sputtering for 30 min under the same conditions. Finally, the graphite modified $LiMn_2O_4$ particles were recovered and fabricated as the electrode as mentioned above.

2.2 Sample charaterizations

The powder X-ray diffraction (XRD, Rint-2000, Rigaku, Japan) using Cu Kα radiation was employed to identify the crystalline phase of the prepared samples. The morphologies of the prepared samples were observed by scanning electron microscope (SEM, JEOL, JSM-5612LV) with an accelerating voltage of 20 kV, and by transmission electron microscope (TEM, Tecnai G12, 200 kV). The surface elemental valence states of the prepared samples were determined by an X-ray photoelectron spectrometer (XPS, Kratos Model XSAM800) equipped with a Mg K_α achromatic X-ray source (1235.6 eV). Before XPS analyses, the samples were sputtered with 4 mm^2 Ar^+ spot (1 KV, 2 μA) to remove the surface, so that the layer under the surface can be analyzed. The contents of Mn dissolved in the electrolyte were determined by inductively coupled plasma-atomic emission spectrometry (ICP-AES, IRIS intrepid XSP, Thermo Electron Corporation).

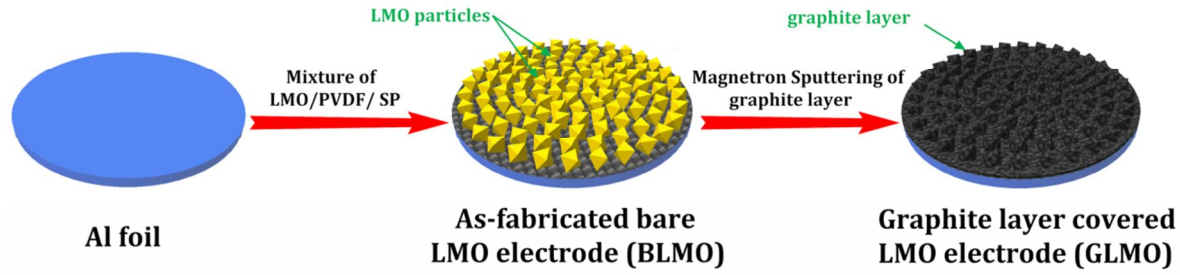

Fig. 1 Schematic diagram of preparation of the nano-thin graphite layer covered $LiMn_2O_4$ electrode.

2.3 Electrochemical performance evaluations

The electrochemical performances of the samples were evaluated using CR2025 coin-type cells composed of the prepared cathode, metallic lithium anode, a commercial polypropylene micro-porous separator (Ube Industries, UP3074, 10 μm in thickness) and 1 mol L^{-1} $LiPF_6$ in ethylene carbonate (EC)/dimethyl carbonate (DMC)/ethyl methyl carbonate (EMC) (1:1:1 v/v/v). The assembly of the cells was carried out in a dry Ar-filled glove box. Electrochemical charge-discharge tests were carried out with Neware battery circler between 3.3 V and 4.35 V at 55 °C. For charging, a constant current (1C rate) was applied until a voltage of 4.35 V was reached, which was then held constant until the current is one tenth of the intial value. For discharging, a galvanostatic condition (1C rate) was conducted until a voltage of 3.3 V was reached.

The electrochemical impedance spectroscopy (EIS) and cyclic voltammetry (CV) measurements were carried out with a CHI660D electrochemical analyzer. The CV curves were collected at the scanning rate of 0.1 mV s^{-1}. The impedance spectra were recorded at discharge state under the open circuit potential (DC bias = 0 mA) by applying an AC voltage of 5 mV amplitude in the 0.01 Hz-100 kHz frequency range.

3 Results and discussion

In order to verify the formation of a graphite layer covering on the surface of the electrode, unmodified and graphite-layer-modified $LiMn_2O_4$ electrodes (sputtering for 30 min) without adding acetylene black and PVDF were prepared and characterized. XRD patterns of $LiMn_2O_4$ cathodes before and after graphite modification are shown in Fig. 2(a). As illustrated in Fig. 2(a), there is no change and no peaks shift after graphite covering, indicating that the crystal structure of the spinel $LiMn_2O_4$ is not affected by the magnetron sputtering process. XPS analyses in different depth in Fig. 2(b) show that the Mn content on the surface (without Ar^+ sputtering) of BLMO is as high as that inside (within Ar^+ sputtering for 1 min), while there are no obvious Mn 2p peaks on the surface of graphite coated $LiMn_2O_4$ electrode, indicating a Mn-free coating layer on the surface of graphite coated $LiMn_2O_4$ electrode.

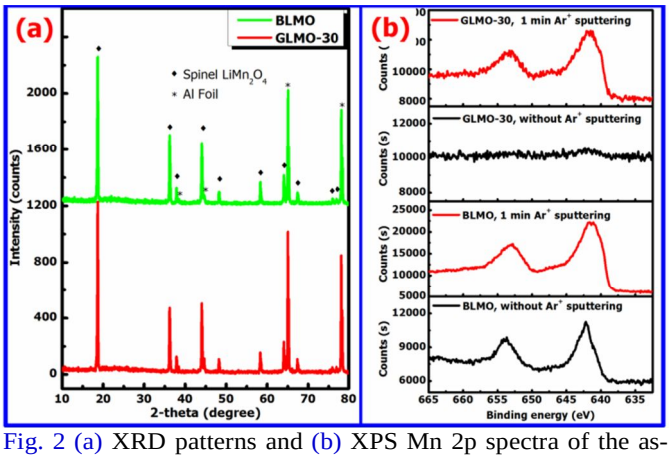

Fig. 2 (a) XRD patterns and (b) XPS Mn 2p spectra of the as-fabricated $LiMn_2O_4$-based electrode in different depth before and after graphite layer modification. Ar^+ sputtering was used to remove the surface so that the inside layer can be detected.

TEM image of the unmodified electrode in Fig. 3(a) shows that the surface of $LiMn_2O_4$ particles is bare, while a covering layer with a thickness of about 50 nm is observed on the surface of $LiMn_2O_4$ particles in the modified electrode, as shown in Fig. 3(b). EDS analysis for the selected region "1" (Fig. 3(c)) shows high contents of elemental Mn and O on the surface of $LiMn_2O_4$ particles with weak signal of carbon which results from the carbon support film. However, EDS analysis for the selected region "2" (Fig. 3(d)) demonstrates much higher content of elemental carbon on the surface, further proving the formation of carbon layer covering on the as-modified $LiMn_2O_4$ cathode. Raman results [Fig. S1, ESI] indicate that the coating layer is mainly graphitic carbon.

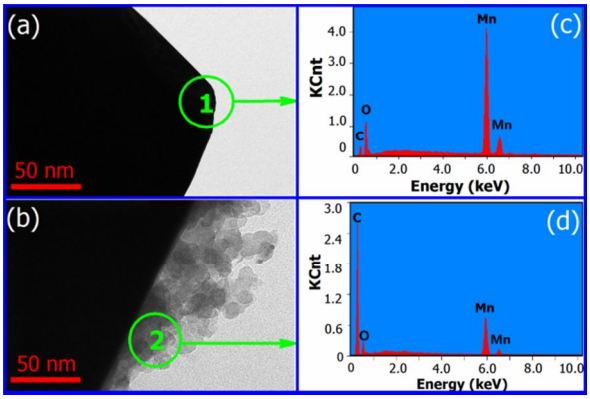

Fig. 3 TEM images of (a) unmodified $LiMn_2O_4$-based electrode (BLMO), and (b) graphite layer modified $LiMn_2O_4$-based electrode (GLMO-30); EDS results in the (c) region "1", and (d) in the region "2".

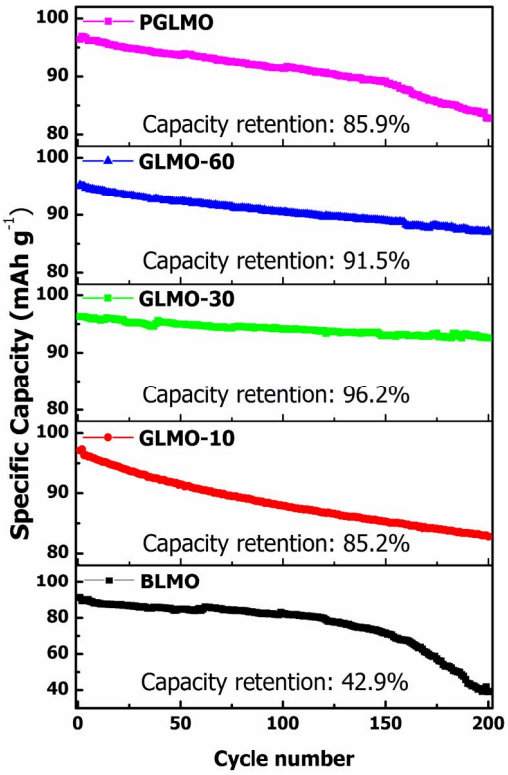

Fig. 4 Cycle performance of BLMO, GLMO-10, GLMO-30, GLMO-60 and PGLMO at 1C rate under 55 °C.

Fig. 4 shows the comparison of cycle performance of the BLMO, GLMO-10, GLMO-30, GLMO-60 and PGLMO at 1C rate (1C=120 mA g^{-1}) under 55 °C. After 200 cycles, the BLMO, GLMO-10, GLMO-30, GLMO-60 and PGLMO exhibit specific capacities of 39, 83, 93, 87 and 83 mAh g^{-1}, maintaining 42.9%, 85.2%, 96.2%, 91.5% and 85.9% capacity retention, respectively. It can be easy to conclude that sputtering for 30 min can obtain the optimal thickness of graphite layer and the GLMO-30 exhibits the better cycle performance than PGLMO when sputtering for the same time. It is noted that the GLMO-60 shows worse cyclability than GLMO-30, which may be due to that too thicker coating layer is bad for Li^+ diffusion especially after the electrolyte decomposes and the decomposed products are formed on the surface of the electrode.

To understand the roles of graphite layer in the improvement of electrochemical performance of $LiMn_2O_4$-based LIBs at elevated temperature, CV and EIS tests were conducted during the elevated–temperature cycling, and XPS, SEM, XRD and ICP-AES analyses were performed after 200 cycles for BLMO and GLMO-30.

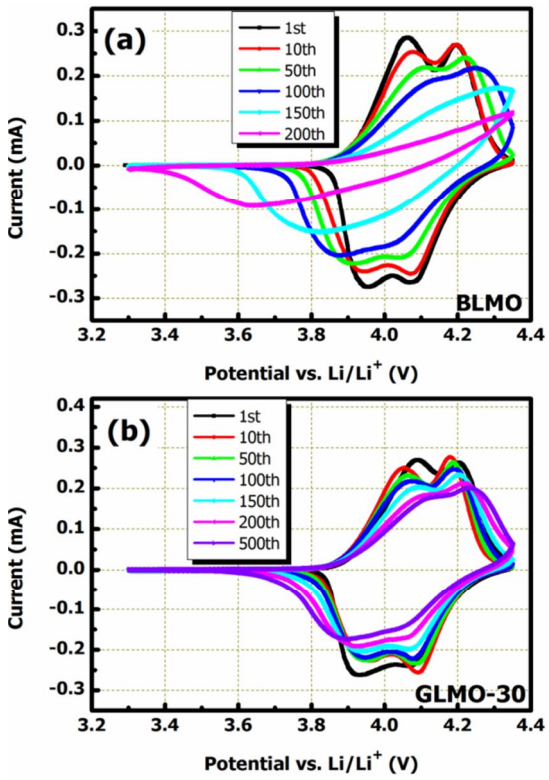

Fig. 5 CV curves of the fabricated cells collected in different cycling at elevated temperature. (a) unmodified $LiMn_2O_4$ electrode (BLMO), (b) graphite layer modified $LiMn_2O_4$ electrode (GLMO-30). Scanning rate: 0.1 mV s^{-1}.

Fig. 5 shows the CV curves of the BLMO and GLMO-30 at 0.1 mV s^{-1} during various cycles. Both samples present two pairs of peaks reflecting the classical redox process of manganese oxide spinel (For the first cycle, in case of BLMO, 4.05 and 4.2 V for oxidation and 3.95 and 4.1V for reduction, and in case of GLMO, 4.1, 4.2V for oxidation and 3.9,4.1V for redoction). In the first cycling, the GLMO-30 shows a little bit higher polarization than BLMO. In subsequent several cycles, the oxidation peaks of BLMO shift right accompanied by the leftward shift of the reduction peaks, indicating worse electrochemical reversibility. While the CV curve of GLMO-30 during the 10th cycle shows a lower polarization compared to that during the 1st cycle. It can be assumed that the graphite covering layer will hinder the Li^+ transmission during the first several cycles for its relatively poor wettability [Fig. S2, ESI] and requirement of long-time activation. If further cycled, both samples demonstrate enlarged $\triangle U_{oxi\text{-}red}$ (the difference of oxidative potential and reductive potential), indicating that the electrode polarization of the electrodes increases as the cycling goes on. However, the CV curves related to GLMO-30 sample are much steadier than that of BLMO sample. Specifically, the BLMO sample shows no typical spinal $LiMn_2O_4$ redox peaks after 150 cycles while the GLMO-30 sample maintains two pairs of classical peaks with only a little a little weaker and wider change during the whole cycle process (500 cycles). The electrode polarization within cycling may be rooted mainly in decomposition of electrolyte and subsequent deposition of poor conductive organic or inorganic species on the surface of electrode under elevated temperature.[7] The HF decomposed from the electrolyte will attack the surface of the $LiMn_2O_4$ particles, which may be another reason for electrode polarization.[8] The GLMO-30 demonstrates much less decrease in electrode polarization than BLMO as the cycling goes on, indicating that the cell composed of graphite layer modified electrode owns dramatically improved chemical stability of the electrode/electrolyte interface, which can suppress the attacking by HF originated from the organic electrolyte. This polarization difference reveals that cycling stability of GLMO-30 is better that BLMO and the graphite covering layer can stabilize the structure of the $LiMn_2O_4$ particles.

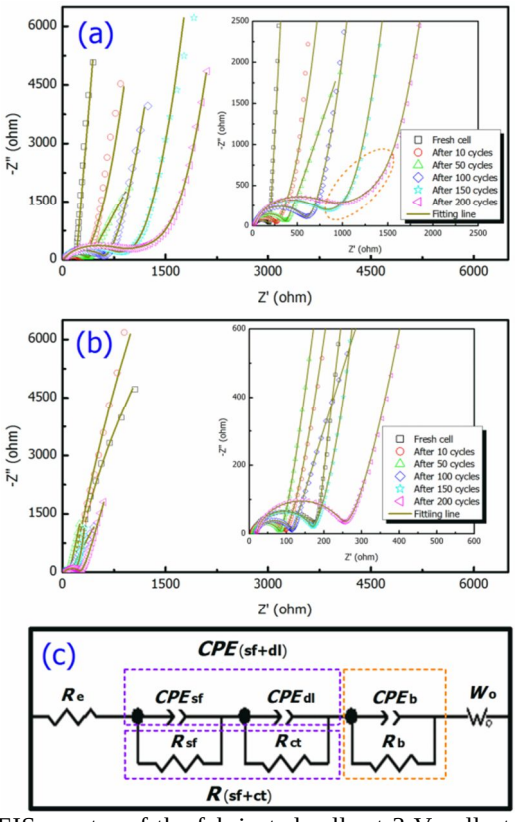

Fig. 6 EIS spectra of the fabricated cells at 3 V collected after different elevated-temperature cycles. (a) Unmodified $LiMn_2O_4$ electrode (BLMO); (b) Graphite layer coated $LiMn_2O_4$ electrode (GLMO-30); Inset (a, b) is the corresponding magnified plot; (c) The equivalent circuit introduced to fit the EIS data.

Table 1 Fitted R_s, $R_{(sf+ct)}$ and R_b values of the as-fabricated BLMO and GLMO-30 electrodes at open-circuit potential after various cycle number under 55 °C

Cycle number	Unmodified $LiMn_2O_4$ electrode			Graphite layer modified $LiMn_2O_4$ electrode		
	R_e (Ω)	$R_{(sf+ct)}$ (Ω)	R_b (Ω)	R_e (Ω)	R_{sf} (Ω)	R_b (Ω)
0 cycle	3	195±2	-	5	178±2	-
10 cycles	3	241±2	-	6	86±2	-
50 cycles	7	356±2	-	9	71±2	-
100 cycles	6	569±2	-	17	100±2	-
150 cycles	9	758±2	175±2	18	149±2	-
200 cycles	11	759±2	667±2	20	227±2	-

The electrochemical impedance spectroscopy (EIS) is a powerful method for studying the electrochemical mechanism of the electrodes.[15, 42] The Nyquist plots of the prepared BLMO and GLMO-30 samples at discharge state after different cycles at elevated temperature are shown in Fig. 6(a) and Fig. 6(b), respectively. The spectra are composed of an intercept at high frequency, one depressed semicircle in the high-to-medium frequency followed by a slope line in low frequency. The intercept corresponds to the ohmic resistance (R_e) of the cell, the semicircle can be assigned to surface film impedance (R_{sf}//CPE_{sf}) as well as charge-transfer impedance (R_{ct}//CPE_{dl}), and the slope line in low frequency is indexed with the Warburg impedance. The EIS data are fitted using the equivalent electrical circuit shown in Fig. 6(c) and the results are shown in Table 1. As can be seen in Table 1, both cells show increased R_s values as the cycling goes on. However, the GLMO-30 sample owns larger values of R_e than BLMO. This is because that the conductivity of the interface is worsened by the poor conductive products formed by electrolyte decomposition.[7] Nevertheless, the R_e is too small to become the controlling step of the electrode process in lithium ion batteries. The semicircle was fitted with a combination of surface-film and charge-transfer resistance $R_{(sf+ct)}$ parallel connecting with $CPE_{(sf+dl)}$ for their overlapping and indistinguishable property. In fresh BLMO and GLMO-30 cells, the $R_{(sf+ct)}$ values show no significant difference. With cycling going on, the $R_{(sf+ct)}$ values of BLMO is found to increase from 195±2 Ω to 759±2 Ω. However, the GLMO-30 shows a decreased $R_{(sf+ct)}$ value during the first 50 cycles and then increases from 71±2 Ω to 227±2 Ω in the last 150 cycles. This phenomenon in GLMO-30 certifies the fact about the poor wettability [Fig. S2, ESI] and requirement of long-time activation of the graphite covering layer. Another reason is that the graphite layer could promote the charge transfer (especially for electron transfer) due to its good electronic conductivity. After 200 cycles, the GLMO-30 demonstrates less than one third of $R_{(sf+ct)}$ compared to BLMO, indicating a more stable electrode/electrolyte interface, which is in favor of Li^+ transmission. This also reflects the better cycle performance of GLMO-30 than that of BLMO.

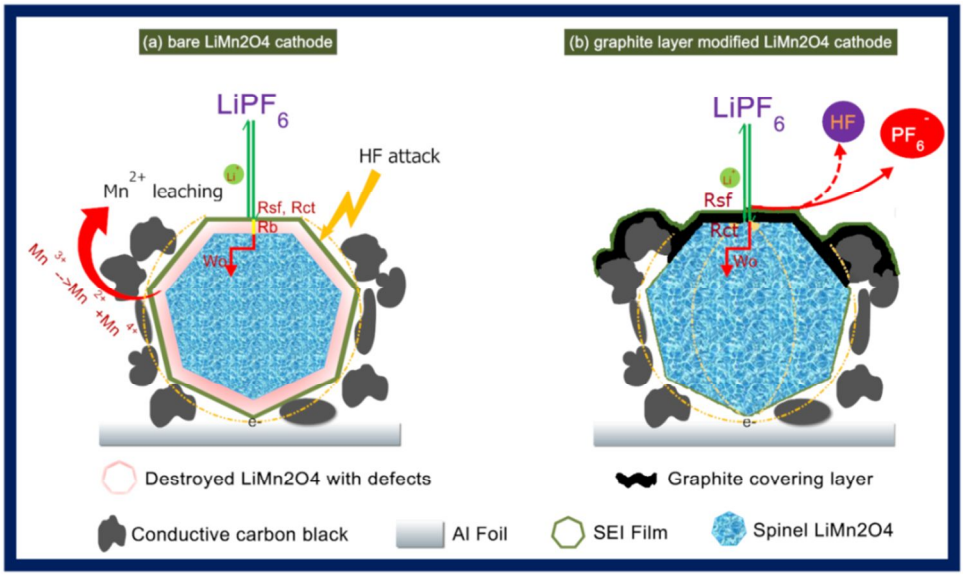

Fig. 7 Schematic conduction/diffusion of electron and lithium ions during the electrochemical kinetics process in the (a) BLMO and (b) GLMO-30 electrode, respectively.

With the cycling going on, the surface of the bare $LiMn_2O_4$ electrode would be destroyed and form numerous lattice defects. The damaged $LiMn_2O_4$ surface layer owns poor conductivity, and thus goes against the subsequent Li^+ diffusion from the interface into the bulk $LiMn_2O_4$ spinel lattices. As a result, the Li^+ ions concentrate in the damaged layer and hinder the operation of the whole electrochemical process. This phenomenon is confirmed in the EIS spectra at the later stage. After 150 cycles, the EIS spectra of the BLMO are composed of an arc at middle-to-low frequency, which can be assumed to be the resistance of Li^+ diffusion through the destroyed $LiMn_2O_4$ layer.[43] It is fitted with a parallel connection of R_b and CPE_b for the first time. The popping up and subsequently rapid increase of R_b in BLMO during cycles, reveals the serious damage of $LiMn_2O_4$ structure by HF. However, the GLMO-30 shows no R_b during the whole cycle, demonstrating that the surface of $LiMn_2O_4$ particles is safe from HF attack under the protection of the graphite cover layer.

Fig. 7 shows the schematic diagram of the electrochemical kinetics process in the BLMO and GLMO-30 electrodes. In the bare cathode, as shown in Fig. 7(a), the electrolyte containing $LiPF_6$ decomposes in according with the following chemical equation (Eq. 1).

$$LiPF_6 \rightarrow LiF+PF_5 \quad (1)$$

Then the formed PF_5 reacts with the non-aqueous solution and HF is produced.[44] When the $LiMn_2O_4$ particles are exposed in the electrolyte, the disproportionation reaction of Mn^{3+} on the surface of $LiMn_2O_4$ particles will be induced and promoted by HF and the produced Mn^{2+} dissolves in the electrolyte. As a result, the MnO_2, as well as probably LiF, is formed on the surface of $LiMn_2O_4$ particles [Eq. (2)], causing the worsening of the surface spinal structure of $LiMn_2O_4$ particles.

$$2LiMn_2O_4+2HF \rightarrow 2LiF+[Mn^{2+}][O^{2-}]+3MnO_2+H_2O \quad (2)$$

The lattices on the surface of $LiMn_2O_4$ are disordered, causing large resistance over the Li^+ diffusion through this region (R_b//CPE_b, surrounded with pink color in Fig. 7(a)) to the bulk lattice. In addition, the electronic conductivity of $LiMn_2O_4$ is decreased, particularly on the surface, which is due to the decrease of Mn^{3+}/Mn^{4+} couple.[45] However, when the $LiMn_2O_4$ cathode is covered with a graphite layer, the $LiMn_2O_4$ particles can be protected from HF attack, as shown in Fig. 7(b). Thus, the surface structure of the $LiMn_2O_4$ particles in GLMO-30 has little change during the elevated-temperature charge-discharge process. There is no extra poor-conductive layer with defects between the SEI film and the bulk $LiMn_2O_4$ being observed.

To further confirm above assumption, investigate the behavior of Mn dissolution at elevated temperature, and evaluate the structural and morphological stabilities of graphite-coated $LiMn_2O_4$ in the electrolyte, the cells after cycling at elevated temperature were disassembled and washed with DMC solvent for three times in the Ar-filled glove box. Then the cathodes were dried and analyzed via SEM, XPS, XRD techniques, respectively. The DMC washing liquor (30 mL) was recovered for ICP analysis.

In order to detect the elemental composition in different depths of the electrodes, the BLMO and GLMO-30 cathodes were under Ar^+ sputtering for different time and the XPS analyses were conducted. Fig. 8 shows the XPS Mn 2p spectra of the BLMO and GLMO-30 electrodes before and after cycles within Ar^+ beam sputtering for different time, respectively. As can be seen in Fig. 8, before Ar^+ ion sputtering, both BLMO and GLMO-30 electrodes show unobvious Mn 2p peaks (Fig. 8(a1), Fig. 7(b1)), indicating that a Mn-deficient layer on the surface of $LiMn_2O_4$ particles is present. This layer can be attributed to the decomposition of the electrolyte and formation of solid-electrolyte interface (SEI) film on the surface of $LiMn_2O_4$ particles. After 1 min Ar^+ sputtering, the intensities of Mn 2p peaks of BLMO are weak (Fig. 8(a2)), indicating low Mn content in this depth, which is due to Mn^{2+} leaching induced by HF attack and SEI composition infiltrating into this region. After 5 min Ar^+ sputtering, the Mn 2p peaks can be observed clearly (Fig. 8(a3)), which reveals that the bulk $LiMn_2O_4$ is exposed in this depth. However, strong intensities of Mn 2p peaks of GLMO-30 in Fig. 8(b2) indicate that the surface coatings (graphite layer as well as probably SEI film) can be easily removed by just 1 min Ar^+ sputtering. The Mn 2p peaks of GLMO-30 don't become more intensive in the further depth (Fig. 8(b3)), revealing good $LiMn_2O_4$ particles safe from damage by HF attack.

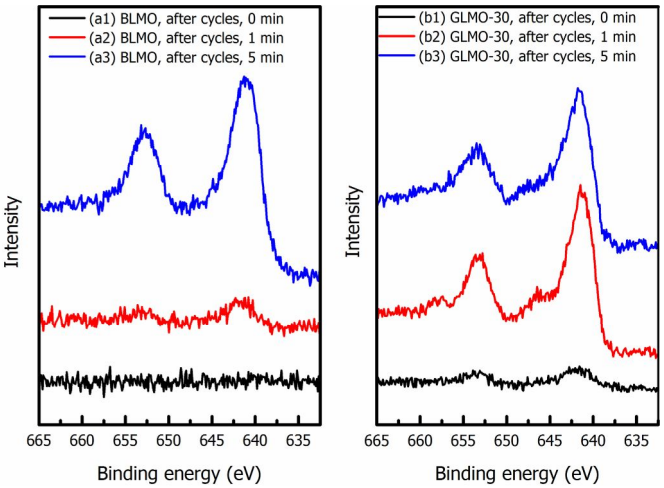

Fig. 8 XPS Mn 2p spectra of the surface of BLMO and GLMO-30 cathode after 200 cycles at 1C rate under the temperature of 55 °C. The samples are under Ar^+ sputtering for (a1, b1) 0 min, (a2, b2) 1 min, (a3, b3) 5 min, respectively, to analyze the layer inside the electrode.

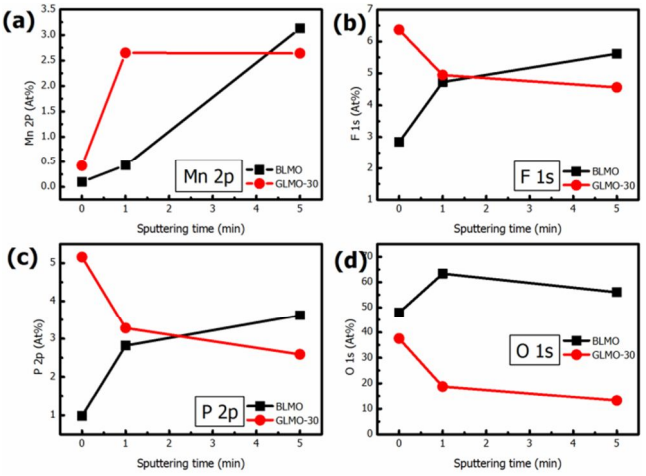

Fig. 9 XPS determined elemental contents of BLMO and GLMO-30 electrode after cycles as a function of sputtering time: (a) Mn 2p, (b) F 1s, (c) P 2p, (d) O 1s.

Fig. 9 shows the contents of Mn 2p (Fig. 9(a)), F 1s (Fig. 9(b)), P 2p (Fig. 9(c)), O 1s (Fig. 9(d)) of cycled BLMO and

GLMO-30 as a function of sputtering depth. Before Ar^+ sputtering, the contents of F 1s, P 2p of BLMO are less than that after 1 min Ar^+ sputtering, indicating the polymerized carbonates are formed on the surface of BLMO electrode,[7] and P_2O_5 and LiF are able to form inside the electrode without graphite coating. In contrast, the contents of F 1s, P 2p, O 1s of GLMO-30 decrease rapidly as a function of sputtering time from 0 to 1min, indicating that, under the protection of graphite layer, most of products originating from the decomposition of electrolyte are effectively intercepted outside the graphite layer. It is noted that, inside the electrodes, the O 1s content of BLMO is much more than that of GLMO-30. It is because that the oxygen-rich products decomposed from the electrolyte are able to infiltrate into the BLMO electrode and lead to leaching of Mn. It also reveals that the graphite layer as a barrier of GLMO-30, performs well in suppressing such infiltration. These differences of elemental contents as a function of sputtering depth reflect the assumption about the differences of electrochemical kinetics process in the BLMO and GLMO-30 electrodes.

Fig. 10 shows the SEM images of the BLMO and GLMO-30 before and after cycles, respectively. Before cycles, both samples have large $LiMn_2O_4$ particles [Fig. 10(a) and Fig. 10(b)]. As seen in Fig. 10(c1), after 200 cycles, the large particles become small and the small particles disappear in BLMO sample, which is due to the Mn dissolution in the electrolyte. The magnified image (Fig. 10(c2)) shows that the cycled $LiMn_2O_4$ particles are broken into small particles without graphite coating. However, the $LiMn_2O_4$ particles in the cycled GLMO-30 cathode maintain the pristine morphology, indicating that, under the protection of graphite layer, the GLMO-30 successfully withstands corrosion of HF during the elevated-temperature cycles.

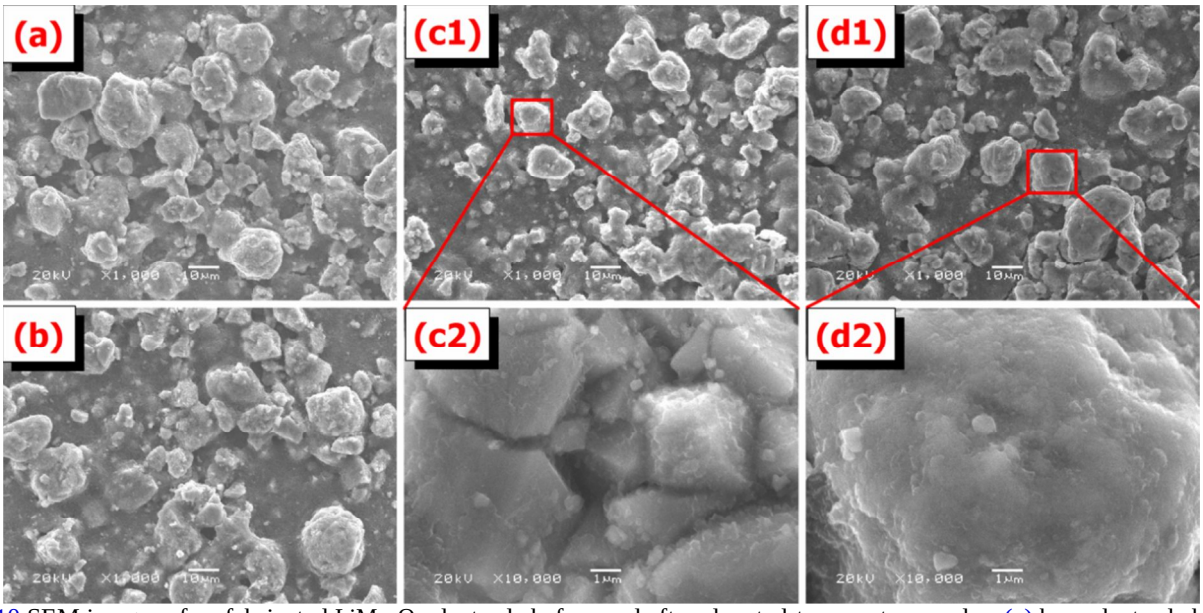

Fig. 10 SEM images of as-fabricated $LiMn_2O_4$ electrode before and after elevated-temperature cycles. (a) bare electrode before cycle, (b) graphite layer modified electrode before cycle, (c1, c2) unmodified electrode (BLMO) after 200 cycles, (d1, d2) graphite layer modified electrode (GLMO-30) after 200 cycles.

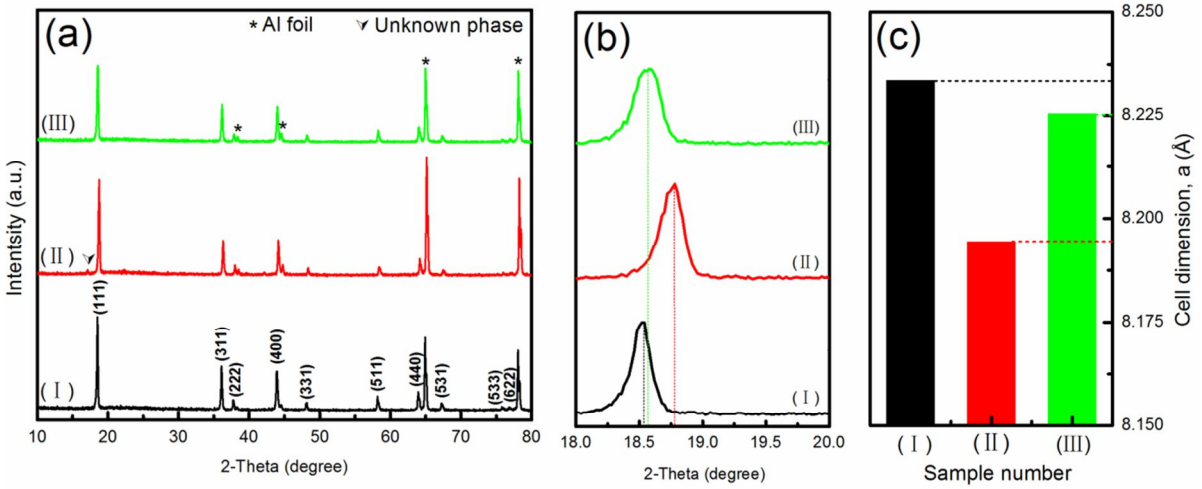

Fig. 11 (a) The XRD patterns, (b) magnified (111) peaks curves and (c) refined cell dimension of the selected samples, (Ⅰ) fresh BLMO cathode, (Ⅱ) BLMO cathode after 200 cycles and (Ⅲ) GLMO-30 cathode after 200 cycles.

Table 2 ICP analyses results of elemental (Li, Mn) contents in the electrode and electrolyte of BLMO and GLMO-30 after 200 cycles at 55 °C

Sample		Fresh $LiMn_2O_4$	Cycled BLMO	Cycled GLMO-30
Li, Mn content in the electrode	Li (wt.%)	4.06	4.48	4.13
	Mn (wt.%)	60.63	57.12	60.27
	Li/Mn mol ratio	1: 1.88	1: 1.61	1: 1.84
Mn contnet in the electrolyte	Mn (ppm)	--	3.4	0.4
	Mn leaching ratio	--	0.261%	0.0241%

XRD analyses of the samples after 200 cycles were conducted for further investigating the structural changes during elevated-temperature cycling process. After cycles, both samples maintain their original spinal structure, as seen in Fig. 11(a). However, in Fig. 11(b), compared to $LiMn_2O_4$ cathode before cycling, the (111) peak of BLMO shifts obviously from 18.52 to 18.77°, while that of GLMO-30 shows much less shift after cycles. As shown in Fig. 11(c), though decreasing for both samples after cycles, the cell parameter *a* (side length of unit cell) of BLMO becomes much smaller than that of GLMO-30. The elevated-angle shifting of (111) peak and the shrinkage of crystal lattice reveal the structural degradation. Therefore, under the protection of the graphite layer, the GLMO-30 shows better structural stability than BLMO cathode.

The degradation of structure and morphology during elevated-temperature cycling is due to the dissolution of Mn, which is the main reason for capacity fading.[32] Thus, it is necessary to compare the Mn dissolution behavior of both samples. As seen in Table 2, the Mn content in the electrolyte for GLMO-30 is one order of magnitude less than that for BLMO, and the Li/Mn ratio of cycled GLMO-30 is as much as that of fresh $LiMn_2O_4$ and is lower than that of BLMO, indicating that the graphite layer is able to effectively supress Mn leaching behavior. This result well reflects the difference between BLMO and GLMO-30 in the aspect of structure, morphology, and electrochemical performance during elevated-temperature cycling process.

4 Conclusions

A general and effective strategy had been introduced to address the severe capacity fading issue of $LiMn_2O_4$ cathode at elevated temperature. The $LiMn_2O_4$ cathode has been successfully modified via directly sputtering a graphite layer on its surface. The graphite layer is believed to act as a physical barrier between the cathode and electrolyte, suppressing the leaching of Mn from the $LiMn_2O_4$ cathode that is induced by HF attack and protecting the $LiMn_2O_4$ particles from morphological and structural degradation. It also helps decrease the electrode polarization and electrochemical impedance during the elevated-temperature cycling. As a result, the as-modified $LiMn_2O_4$-based cathodes possess superior cycling performance at elevated temperature. Sputtering for 30 min can obtain the optimal thickness (~50 nm) of the graphite coating layer and GLMO-30 exhibits the best cycle performance at 55 °C. A model for the electrochemical kinetics process is suggested for explaining the roles of graphite layer by introducing an impedance (R_b//CPE_b) over the Li^+ diffusion through a lattice-defective region, which further confirms that the graphite layer coating can avoid the formation of the lattice-defective region by suppressing the Mn dissolution and thus alleviate the severe dissolution of manganese ions into electrolyte.

Acknowledgements

This work was financially supported by the National Basic Research Program of China (973 Program, 2014CB643406), Major Special Project of Science and Technology of Hunan Province, China (No. 2011FJ1005), and the Fundamental Research Funds for the Central Universities of Central South University (2014zzts026).

Notes and references

[a] School of Metallurgy and Environment, Central South University, 932, South Lushan Road, Changsha, P.R. China, 410083.
[b] Department of Mechanical and Biomedical Engineering, City University of Hong Kong, 83 Tat Chee Avenue, Kowloon, Hong Kong.

† Electronic Supplementary Information (ESI) available: [Raman spectra of samples before and after 30 min graphite sputtering; Video images presenting the electrolyte dispersion into the BLMO and GLMO-30 electrodes as a function of time]. See DOI: 10.1039/b000000x/

[1] T.J. Patey, R. Buchel, M. Nakayama, P. Novak, Phys. Chem. Chem. Phys. 11 (2009) 3756.
[2] V. Etacheri, R. Marom, R. Elazari, G. Salitra, D. Aurbach, Energ. Environ. Sci. 4 (2011) 3243.
[3] W. Sun, F. Cao, Y. Liu, X. Zhao, X. Liu, J. Yuan, J. Mater. Chem. 22 (2012) 20952.
[4] D.K. Lee, S.C. Han, D. Ahn, S.P. Singh, K.S. Sohn, M. Pyo, ACS Appl. Mater. Interfaces 4 (2012) 6842.
[5] Q. Tong, Y. Yang, J. Shi, J. Yan, L. Zheng, J. Electrochem. Soc. 154 (2007) A656.
[6] C.C. Chen, K.-F. Chiu, K.M. Lin, H.C. Lin, C.-R. Yang, F.M. Wang, J. Electrochem. Soc. 158 (2011) A262.
[7] T. Eriksson, A.M. Andersson, C. Gejke, T. Gustafsson, J.O. Thomas, Langmuir 18 (2002) 3609.
[8] M. Hirayama, H. Ido, K. Kim, W. Cho, K. Tamura, J.i. Mizuki, R. Kanno, J. Am. Chem. Soc. 132 (2010) 15268.
[9] P.C. Goonetilleke, J.P. Zheng, D. Roy, J. Electrochem. Soc. 156 (2009) A709.
[10] D.-Q. Liu, X.-Q. Liu, Z.-Z. He, Mater. Chem. Phys. 105 (2007) 362.
[11] Y. Dai, L. Cai, R.E. White, J. Electrochem. Soc. 160 (2012) A182.
[12] Y.J. Lee, S.-H. Park, C. Eng, J.B. Parise, C.P. Grey, Chem. Mater. 14 (2002) 194.
[13] J.T. Son, H.G. Kim, J. Power Sources 147 (2005) 220.
[14] Y.L. Ding, J. Xie, G.S. Cao, T.J. Zhu, H.M. Yu, X.B. Zhao, J. Phys. Chem. C 115 (2011) 9821.
[15] A. Sakunthala, M.V. Reddy, S. Selvasekarapandian, B.V.R. Chowdari, P.C. Selvin, Electrochim. Acta 55 (2010) 4441.
[16] M. Prabu, M.V. Reddy, S. Selvasekarapandian, G.V. Subba Rao, B.V.R. Chowdari, Electrochim. Acta 88 (2013) 745.
[17] X. Li, R. Yang, B. Cheng, Q. Hao, H. Xu, J. Yang, Y. Qian, Mater. Lett. 66 (2012) 168.
[18] M. Prabu, M.V. Reddy, S. Selvasekarapandian, S. Admas, K.P. Loh, G.V.S. Rao, B.V.R. Chowdari, J. Electrochem. Soc. 160 (2013) A3144.
[19] L. Xiong, Y. Xu, T. Tao, X. Du, J. Li, J. Mater. Chem. 21 (2011) 4937.
[20] L. Yu, X. Qiu, J. Xi, W. Zhu, L. Chen, Electrochim. Acta 51 (2006) 6406.
[21] C.Y. Ouyang, X.M. Zeng, Z.Sljivancanin, A. Baldereschi, J. Phys. Chem. C 114 (2009) 4756.
[22] D. Guan, J.A. Jeevarajan, Y. Wang, Nanoscale 3 (2011) 1465.

[23] J. Zhao, G. Qu, J.C. Flake, Y. Wang, Chem. Commun. 48 (2012) 8108.
[24] J. Zhao, Y. Wang, J. Solid State Electr. 17 (2012) 1049.
[25] J. Zhao, Y. Wang, J. Phys. Chem. C 116 (2012) 11867.
[26] J. Zhao, Y. Wang, Nano Energy 2 (2013) 882.
[27] K.Y. Chung, C.-W. Ryu, K.-B. Kim, J. Electrochem. Soc. 152 (2005) A791.
[28] S.-T. Myung, K. Amine, Y.-K. Sun, J. Mater. Chem. 20 (2010) 7074.
[29] H. Li, H. Zhou, Chem. Commun. 48 (2012) 1201.
[30] T.-F. Yi, Y.-R. Zhu, X.-D. Zhu, J. Shu, C.-B. Yue, A.-N. Zhou, Ionics 15 (2009) 779.
[31] S.-C. Park, Y.-M. Kim, Y.-M. Kang, K.-T. Kim, P.S. Lee, J.-Y. Lee, J. Power Sources 103 (2001) 86.
[32] S.-C. Park, Y.-M. Kim, S.-C. Han, S. Ahn, C.-H. Ku, J.-Y. Lee, J. Power Sources 107 (2002) 42.
[33] J.M. Tarason, M. Armand, Nature 414 (2001) 359.
[34] X. Luan, D. Guan, Y. Wang, J. Nanosci. Nanotech. 12 (2012) 7113.
[35] A. Ponrouch, A.R. Goñi, M.T. Sougrati, M. Ati, J.-M. Tarascon, J. Nava-Avendaño, M.R. Palacín, Energ. Environ. Sci. 6 (2013) 3363.
[36] H. Xia, Z. Luo, J. Xie, Prog. Nat. Sci. 22 (2012) 572.
[37] S. Lee, Y. Cho, H.K. Song, K.T. Lee, J. Cho, Angew. Chem. Int. Ed. Engl. 51 (2012) 8748.
[38] X.-M. Liu, Z.-D. Huang, S. Oh, P.-C. Ma, P.C.H. Chan, G.K. Vedam, K. Kang, J.-K. Kim, J. Power Sources 195 (2010) 4290.
[39] S.J. Shi, J.P. Tu, Y.J. Mai, Y.Q. Zhang, C.D. Gu, X.L. Wang, Electrochim. Acta 63 (2012) 112.
[40] J. Wang, Q. Zhang, X. Li, Z. Wang, K. Zhang, H. Guo, G. Yan, B. Huang, Z. He, Electrochem. Commun. 36 (2013) 6.
[41] P.J. Kelly, R.D. Arnell, Vacuum 56 (2000) 159.
[42] K.S. Tan, M.V. Reddy, G.V.S. Rao, B.V.R. Chowdari, J. Power Sources 141 (2005) 129.
[43] Q.C. Zhuang, S.D. Xu, X.Y. Qiu, Y.L. Cui, L. Fang, S.G. Sun, Prog. Chem 22 (2010) 1044.
[44] X. Wu, Z. Wang, X. Li, H. Guo, Y. Zhang, W. Xiao, J. Power Sources 204 (2012) 133.
[45] J. Marzec, K.S. wierczek, J. Przewoznik, J. Molenda, D.R. Simon, E.M. Kelder, J. Schoonman, Solid State Ionics 146 (2002) 225.